HHS Public Access

Author manuscript

Int J Min Sci Technol. Author manuscript; available in PMC 2020 July 01.

Published in final edited form as:

Int J Min Sci Technol. 2020 ; 30(2): 157–166. doi:10.1016/j.ijmst.2020.01.006.

Numerical simulation of roof cavings in several Kuzbass mines using finite-difference continuum damage mechanics approach

Mikhail Eremin[a,*], **Gabriel Esterhuizen**[b], **Igor Smolin**[a,c]

[a]Institute of Strength Physics and Materials Science, Siberian Branch, Russian Academy of Sciences, Tomsk 634055, Russian Federation

[b]National Institute for Occupational Safety and Health, Pittsburgh, PA 15236, USA

[c]National Research Tomsk State University, Tomsk 634050, Russian Federation

Abstract

An essential stage of mine design is an estimation of the steps of the first and periodic roof caving in longwall mines. Generally, this is carried out using the field experience and can be much enhanced by numerical simulation. In this work, the finite-difference method was applied coupled with the continuum damage mechanics (CDM) approach to simulate the stress-strain evolution of the rock mass with the underground opening during coal extraction. The steps and stages of roof caving were estimated relying on the numerical simulation data, and they were compared with the field data from several operating mines in the south of the Kuznetsk Basin, Russia. The dependence of the first roof caving step in simulation linearly correlates with field data. The results correspond to the actual roofs of longwall panels of the flat-dipping coal seams and the average rate of face advancement is approximately 5 m/day.

Keywords

Longwall mining; Rock mass; Underground openings; Roof caving; Abutment pressure; Numerical simulation

1. Introduction

Longwall mining is one of the two most common methods of underground coal extraction in the world. It is quite safe, highly productive, and demands fewer operating personnel number, etc. And it is more appropriate for coal seams with low dip angles (flat-dipping) and rectangular-shaped minefields. Large cantilevers of the main roof might be left behind the

*Corresponding author. eremin@ispms.tsc.ru (M. Eremin).

Declaration of Competing Interest

Authors declare no conflict of interest concerning any part of work.

wall face (about 100 m or more) in certain geological conditions (usually with large main-roof thicknesses) if no special roof caving procedures are applied. This amplifies the abutment pressure in front of the cutting face by 2–2.5 factors compared to the vertical stress value in the case where the gob is about 100 m long [1,2]. The maximum value of abutment pressure is observed several meters deep into the intact coal seam. At the same time, 1.5–3 m along the strike the coal yields, occasionally causing breaks of mining due to outbursts [3]. Underground openings disturb the virgin state of stress and strain [4]. Stress enhancement in the vicinity of openings is responsible for the manifestation of rock, coal and gas bursting, immediate roof crushing into the working zone, the unsustainability of protective pillars, etc. [5].

Numerous field observations show that the fracture of rock-mass elements near the opening is generally related to the periodic character of the stress state. Its periodicity is caused by roof cavings. Each caving gradually increases the height of a fracture-rich zone until it becomes stable. The arch-shaped, fracture-rich zone is formed above the extracted panel [6]. In terms of the damage degree, the overlying strata are conventionally divided into caved, fractured, and continuous deformation zones [3,4]. The heights of fractured strata (H_{fs}) is about several times of the average thickness of coal seams (H_m): $H_{fs} \approx kH_m$, where k according to the different researches is in the range of 25–30, 2–48 and 20–100, depending on different geological and geotechnical conditions [7–9]. An essential stage of mining management is an estimation of the first and periodic steps of roof caving. These estimations are generally based on the working personnel experiences, empirical engineering formulas, geological observations of caving process, the state of stress and strain evolution in similar geological conditions, etc. In recent years, the attempts of physical modeling on equivalent materials and numerical simulations (e.g. UDEC, FLAC3D, ANSYS, CosFlow, PHASE2, LaModel packets) have been made to estimate different parameters of the coal mining process and investigate the evolution of the state of stress and strain parameters [2–19]. This is due to the ability of numerical simulation to give a deeper insight into the state of stress and strain parameters, the disintegration of rocks, permeability, interaction between the strata and support systems, estimation of sustainability of the pillars and gates, etc. A profile borehole investigation of geological conditions of the Kuznetsk Basin coal seams showed that the main roof is commonly composed of siltstone and sandstone and has different layer thicknesses up to 60–80 m. A thick main roof of strong sandstone yields the accidents and unexpected roof failures [19]. In some cases, there is no first roof caving at relatively small face retreat distances, which yields high values of vertical stress concentration and mining safety hazard. Thus, the critical lengths of mined-out space have to be estimated to develop the recommendations for roof caving and abutment pressure management. In this paper, the finite-difference approach is applied to simulate the stress-strain evolution of the rock mass with an underground opening at a constant rate of face advancement. The initial state of the rock mass is the result of gravity forces. A structural model of rock mass was built containing an underground opening on the basis of a simplified borehole log of the Kondomsky deposit. And the steps of the first and periodic caving of the main roof and the stages of caving (involving the overlying strata) were estimated.

2. Geological conditions of several coal seams of the Kuznetsk Basin

The Kuznetsk Basin (frequently referred to as Kuzbass) is located in southwestern Siberia, Russia (Fig. 1). Geographically Kuzbass is located between two orogenic systems–Salair Ridge and Kuznetsky Alatau. This geographical position has determined the features of the present-day sedimentary rock bedding. The sedimentary rocks (including coal seams) are located near the orogenic systems experienced large plastic deformations during the post-sedimentary period, and the mining is mostly carried out with an open-pit technology (e.g. in the Belovsky and Batschatsky deposits). However, the coal deposits in the middle and southern parts of Kuzbass have relatively flat-dipping coal seams, where the longwall mining is quite applicable (e.g. the Kondomsky, Baidaevsky, Osinovsky, and Erunakovsky deposits). Fig. 2 shows a conventional division of Kuzbass into the exploration districts. A simplified stratigraphic column of the Kondomsky deposit is also presented in Fig. 2. The Usyatskaya P_1us, Kemerovskaya P_1km, Ishanovskaya P_1i, and Promezhutochnaya P_1p subformations refer to Upper Balahonskaya stage (Kondomsky borehole log, Fig. 2). The roofs of certain coal seams of the Promezhutochnaya and Ishanovskaya subformations represent thick (up to 60–80 m) sandstone layers. In the top part of the Upper Balahonskaya formation, the periods of sedimentation are shorter, so the roof layer thickness is not so large (1–10 m), and alternation of layers is more frequent.

3. Numerical simulation

3.1. Governing equations

In order to solve the problem of the stress-strain evolution of rock mass during the extraction of coal, the numerical integration of the system of solid mechanics equations was performed in a dynamic formulation using the finite difference method. The latter requires some explanation. Generally, the stress-strain evolution of rock mass undergoes quasi-static conditions, i.e. the kinetic energy is negligible, all elements of rock mass are in a quasi-static equilibrium, and strain rates are meagre. However, roof cavings are dynamic phenomena characterized by high strain rates. Thus, both tendencies, i.e. the quasi-static equilibrium between the cavings and the intensification of the deformation process during them, need to be properly described. An intrinsic property of a dynamic formulation is a description of deformation processes with strain rates that cannot be disregarded [22]. For low strain rates, a special technique of slow loading is applied. The gob is increased in a manner so as to maintain quasi-static conditions of rock-mass elements, i.e. every other face advancement step is made once per several thousands of integration time steps to maintain the quasi-static condition of the free surface in the gob area [19,23].

The system of equations includes the laws of mass (Eq. (1)) and momentum (Eq. (2)) conservation written in the Lagrangian form:

$$\rho V = \rho_0 V_0 \tag{1}$$

$$\rho \dot{v}_i = \sigma_{ij,j} + \rho F_i \tag{2}$$

where ρ_0 and ρ is the reference and current value of density, respectively; V_0 and V the reference and current values of volume, respectively; v_i the components of velocity vector; σ_{ij} the components of Cauchy stress tensor; and F_i the components of mass force.

The system also includes the geometrical relations for strain rate and vorticity tensors (Eqs. (3) and (4)):

$$2\dot{\varepsilon}_{ij}^{T} = v_{i,j} + v_{j,i} \tag{3}$$

$$2\dot{\omega}_{ij} = v_{ij} - v_{j,i} \tag{4}$$

where ε_{ij} is the strain tensor.

3.2. Constitutive equations

It is evident in Fig. 2 showing a typical borehole log that the structure of rock mass is presented by many bedding planes of different rocks. The rocks, especially the rock mass, generally have considerable anisotropy of the physical and mechanical characteristics. There are several ways for simulating the state of stress and strain of rock mass under the action of different forces; one is to explicitly consider structural inhomogeneity and input the features of bedding into the model, supposing that the rock material between the bedding planes is isotropic. Following this way, a quasi-isotropic model of the rock mass was constructed, and the complexity of mechanical behaviour description of rocks was reduced, because only two constants in the equation of state, which could be readily obtained from the corresponding experiments, are needed for the description of elastic behaviour of isotropic materials. Also, at the depths of <1 km, where the majority of operating mines are located, the values of vertical stress are relatively lower than those obtained, e.g. under impact loading; thus a linear law relating the components of stress and strain rate tensors–equations of hypoelastic media can be used.

The volumetric and deviatoric parts of the stress tensor can be separated, and hence the hypoelastic media relations are written in the following forms (Eqs. (5) and (6) for volumetric and deviatoric parts, respectively):

$$\dot{P} = -K\left(\frac{\dot{V}}{V} - \dot{\theta}^{P}\right) \tag{5}$$

$$\dot{S}_{ij} + S_{ik}\dot{\omega}_{kj} - S_{kj}\dot{\omega}_{ik} = 2\mu\left[\dot{\varepsilon}_{ij}^{T} - \frac{1}{3}\left(\frac{\dot{V}}{V} - \dot{\theta}^{P}\right)\delta_{ij} - \dot{\varepsilon}_{ij}^{\mathrm{P}}\right] \tag{6}$$

where P is the hydrostatic pressure; K the bulk modulus; S_{ij} the components of deviatoric stress tensor; μ the shear modulus; ε_{ij}^{P} the components of inelastic strain tensor; and θ and θ^{P} the volumetric elastic and inelastic strains, respectively.

The Jaumann corotational derivative is applied in Eq. (6) in order to subtract the rotation of a cell (particle or element of the medium) as a whole. Inclusion of the corotational derivative

is dictated by the fact that the local rotation of element (cell) due to plastic deformations might be very strong in the band of localized inelastic deformation. Thus, to obtain the correct estimations of stress, one needs to subtract the rotation. The total strain consists of two parts: the elastic part (ε_{ij}^{E}) and the inelastic part (ε_{ij}^{P}), so that $\varepsilon_{ij}^{T} = \varepsilon_{ij}^{E} + \varepsilon_{ij}^{P}$.

3.3. Plasticity

It should be mentioned that inclusion into consideration of inelastic deformation of rock-mass elements is of great importance. When the coal seam is mined out, the virgin stress state is violated. This leads to considerable inhomogeneity and nonstationarity of the stress state of rock-mass elements, especially those near newly formed cavities, gateways, mining face, pillars, etc. In these regions of stress amplification, the rocks lose their stability and transit to the inelastic state and sometimes fracture, achieving a residual state [4]. Thus, a mathematical model should include the constitutive equations for inelastic strains and fracture of rocks. In this work, inelastic deformation of rock-mass elements is described by the modified Drucker-Prager model with a non-associated flow rule [24]. The inelastic strain rate tensor components are defined according to the Nikolaevskii plastic potential (Eq. (8)) from the theory of plasticity (Eq. (7)) [25–29]:

$$\dot{\varepsilon}_{ij}^{P} = \dot{\lambda}\frac{\partial g(\sigma_{ij})}{\sigma_{ij}} \tag{7}$$

$$g(\sigma_{ij}) = J_2 - \Lambda P(2Y + \alpha P) + const \tag{8}$$

where $\dot{\lambda}$ is the multiplier used in theory of plasticity; $g(\sigma_{ij})$ the equation of plastic potential; J_2 the second invariant of deviatoric stress tensor; and Λ the dilatancy factor.

Then, the following equation for the inelastic strain rate tensor components can be obtained:

$$\dot{\varepsilon}_{ij}^{\mathrm{P}} = \left(S_{ij} + \frac{2}{3}\Lambda\left(Y - \frac{\alpha}{3}J_1\right)\delta_{ij}\right)\dot{\lambda}, \dot{\theta}^{P} = \dot{\varepsilon}_{ii}^{P} \tag{9}$$

where α is the internal friction factor; and J_1 the first invariant of stress tensor.

Usage of the non-associated flow rule gives an independent rate of dilatancy from internal friction coefficient and describes more precisely the behaviour of rocks. A comprehensive review and a choice of dilatancy parameters of rocks can be found in [30]. In this work, the fact is ignored that the dilatancy factor of rocks strongly depends on confinement stress and accumulated inelastic strain. An interval was selected:

$$\Lambda = const = \tan\left(\frac{\varphi_{\exp}}{8}\right) - \tan\left(\frac{\varphi_{\exp}}{4}\right) \tag{10}$$

where $\varphi_{\exp}$ is an internal friction angle in the Coulomb-Mohr criterion.

Eq. (10) is a satisfactory assumption for the purpose of this work and is consistent with the recommendations on the choice of dilatancy factor by Hoek and Brown [31]. The multiplier

$\dot{\lambda}$ is defined in the calculations when Eq. (11) is satisfied (Drucker-Prager conical yield surface).

$$\begin{cases} f(\sigma_{ij}, D) = -\alpha P + \sqrt{J_2} - Y \\ Y = Y_0(1 - D) \end{cases} \tag{11}$$

where $f(\sigma_{ij}, D)$ is the equation of yield surface; Y_0 and Y the reference and current values of "cohesion", respectively; and D the damage measure.

When deriving the non-associated plastic flow rule, a procedure of stresses correction can be inserted into the available solver [25].

It is notable that both α and Y are the material constants associated with rock cohesion and internal friction angle of Coulomb-Mohr criterion within the Drucker-Prager model [24]. For simplicity, α is further referred to as the internal friction factor and Y the cohesion.

3.4. Damage and fracture

In order to describe the fracture process of rock-mass elements, the theory of continuum damage mechanics (CDM) is applied in this work. The basic ideas and equations of CDM were formulated by Kachanov and Rabotnov [32,33]. The damage process of material was treated as a progressive loss of continuity under applied stresses. Further, a correlation between the damage and fracture mechanics was revealed on the basis of thermodynamics, and it was shown elsewhere that these theories were equivalent [34,35]. The applicability of CDM was demonstrated in many works for different materials, media, and loading conditions, etc [29,35]. The following kinetic equation for the damage measure time derivative is used in this work:

$$\begin{cases} \dfrac{dD}{dt} = \dfrac{(\sigma - \sigma_0)^2}{(\sigma^*)^2 t^*} \\ \sigma = -\alpha P + \sqrt{J_2} \end{cases} \tag{12}$$

where σ_0 and σ is the threshold and Drucker stress in the damage measure, respectively; and σ^* and t^* the model parameters. The model under development was earlier validated against the experiment by consideration of several simple model cases [36–38].

The parameters of the proposed model of damage accumulation are discussed below in detail. The damages start accumulating if $\sigma > \sigma_0$; otherwise, there is no damage accumulation and $D = 0$. It is evident that σ_0 is the threshold stress for damage initiation. The big question is: what is the threshold? By the trial and error method, we found the solution to this problem. All types of stress state are conditionally "located" between the uniaxial tension and uniaxial compression. Thus, for pressure-sensitive materials, the threshold is:

At negative pressure:

$$\sigma_0 = \sigma_t\left(\frac{1}{\sqrt{3}} + \frac{\alpha}{3}\right) \tag{13}$$

And at positive pressure:

$$\sigma_0 = \sigma_c\left(\frac{1}{\sqrt{3}} - \frac{\alpha}{3}\right) \tag{14}$$

where σ_t is the uniaxial tensile strength (UTS); and σ_c the uniaxial compressive strength (UCS).

These two values of σ_0 are the Drucker stress values at uniaxial tension and at uniaxial compression, respectively [24]. If the values of σ_t and σ_c are substituted into Eqs. (13) and (14), then σ_0 at positive and negative pressure equals Y, respectively. In other words, the yield surface would, in this case, coincide with the surface of damage accumulation. However, our simulations showed that in the case of coincidence of yield and damage initiation surfaces, the rocks tend to behave much too viscous at chosen parameters, which contradicts with the observations in mines.

Then, the experiments on the determination of tensile and compressive strengths of rocks were looked through (the experimental values are related to laboratory scale specimens, Table 1). Fig. 3a illustrates the yield surface for the case where the experimental cohesion (Y_{exp}) and experimental internal friction factor (α_{exp}) are taken as the basic strength characteristics of the Drucker-Prager model (grey line in Fig. 3a). The uniaxial tensile strength ($\sigma_{t,DP}$) was calculated from cohesion and internal friction factor (blue dashed line in Fig. 3a) by using the well-known formula [24]. At the same time, the value of tensile strength (red dashed line in Fig. 3a) was experimentally obtained. It can be seen that $\sigma_{t,DP} > \sigma_{t,\text{exp}}$, i.e. the calculated value $\sigma_{t,DP}$ is an overestimated value of tensile strength (see the comparison of these two values for all rocks in Table 1). Overestimation of tensile strength by Drucker-Prager criterion is also mentioned in [39]. Other physical–mechanical properties of rocks necessary for numerical simulation are listed in Table 2 [40].

Thus, the fracture criterion has to be updated. If the elastic stress path No. 1 occurs (dark yellow dashed and dotted lines in the Fig. 3a), no damage is accumulated; but if the pressure becomes less than $-\sigma_{t,\text{exp}}/3$, the cell is fractured (we immediately ascribe $D = 1$ in this case, tensile cut-off).

If we perform a backward calculation and take experimental values of $\sigma_{t,\text{exp}}$ and $\sigma_{c,\text{exp}}$ as basic strength characteristics of the Drucker-Prager model and calculate cohesion (Y_{DP}) and internal friction factor (α_{DP}), two inequations can be obtained: $Y_{DP} < Y_{\text{exp}}$ and $\alpha_{DP} > \alpha_{\text{exp}}$. In our opinion, such a misfit between the calculated parameters and experimental data is accounted for by different mechanisms of deformation of rocks at uniaxial and multiaxial loading, which is revealed by the corresponding experiments. In other words, UCS and UTS are useful in determining the strength envelope in the region of negative pressure and thus allow the entire description of rock behavior to be completed.

The new surface (purple line in Fig. 3a) is built in terms of Y_{DP} and α_{DP}. This surface was proposed in the 2D Haigh-Westergaard stress space to be the surface of damage accumulation onset. Thus, the stress difference (σ–σ_0) in the numerator of Eq. (12) equals $-\alpha_{DP}P + \sqrt{J_2} - Y_{DP}$. If the elastic stress path No. 2 is taken (green dash-dot line in Fig. 3a), damages start accumulating when the new surface is reached. The damage accumulation onset is schematically marked with a circle. After that point, σ–$\sigma_0 > 0$. If $D = 1$, then the cell is fractured and the strength of rocks turns to residual.

Degradation of rock properties in the regions of compressive stress demands a detailed investigation, however this discussion is omitted herein since the fracturing of rock mass elements usually occurs in the regions where tensile stress prevails. In other words, in the framework of the model only shear plastic strains can accumulate rather than damages if the yield criterion is satisfied in the regions of positive pressure $P > 0$ (Fig. 3b). Such an approach is applicable since the crack opening is impossible at high compressive stress values.

In fact, a piece-wise linear approximation of yield strength envelope of rocks with three segments was proposed. If compared to the review of experiments on rock yield strength envelopes reported by Hoek and Martin, then it might be a compulsory assumption [41]. A typical parabolic yield strength envelope is approximated by a piecewise linear function with several segments, which derivation is practically easier for the determination of inelastic strain tensor components.

The critical stress σ^* in the denominator of Eq. (12) is equal to initial values of $\sigma_{t,\mathrm{exp}}$ and $\sigma_{c,\mathrm{exp}}$ for tension and compression, respectively.

The rate of damage accumulation is controlled by the parameter t^*, which is the only adjustable parameter of the proposed model. It has the physical meaning of the characteristic time of a fracture incubation process, while in our model it is a fitting constant. The value of t^* was selected on the basis of the field observations data available from different mines of the Kondomsky deposit, e.g., if the average value of the first roof caving, in particular, geotechnical conditions according to field data is equal to the step of the first main roof caving (L_{fc}), then t^* is selected to make the step of the first in the calculations close to L_{fc}. Table 3 summarizes the field data from 4 mines of the southern Kuzbass. These values were used for the selection of t^* in simulation. Thus, t^* is an empirically derived parameter based on the analysis of the rock response in the Kuzbass coal mines. It might be taken as the field time of first caving expressed in terms of arbitrary units (numerical integration time).

The material after its fracture at this point no longer resists tensile stresses (all stress tensor components are nullified) but resists shear and compressive stresses with local strength $\tau = \alpha_{\mathrm{exp}}P$.

3.5. Structural model of rock mass and initial and boundary conditions

The geological data shows that the average thickness (M) of the Kuzbass working coal seams is within the range of 2–3 m. In this work, several coal seams with the working heights $H_m > 1$ m were taken as case studies. The burial depths of all working seams of the

Kondomsky deposit vary along the exploration lines, according to [21]. In order to estimate the steps of main roof bed weightings for different seams, for the model, the burial depth of the seams was selected under consideration from the field data range. Generally, the lengths of longwall panels vary from 1 to 4 km. It is not, however, necessary to simulate the opening of such a length; moreover, this demands large computing power. Previous calculations and literature data show that it is enough to simulate at best about 200 m of the face advancement in order to understand the features of damage accumulation, abutment pressure amplification, and evolution of other parameters of the state of stress and strain. It was also found out that the lateral and vertical dimensions of the model have to be at least 2 or 3 times bigger (about 400 and 600 m, respectively) than those of the gob (about 200 m), which would allow decreasing the boundary effects. Fig. 4 shows a 2D roof and floor structural model and a loading and mining scheme for Seam 9a (as an example) of the Kondomsky deposit. The locations of longwall face retreat onset and finish are shown by white quads, with the distance between them being 200 m.

The following boundary conditions were applied to the model:

$$\begin{cases} v_y = 0, x_i \in B_1 \\ v_x = 0, x_i \in B_2, B_4 \\ \sigma_{ij} n_j = \sigma_{\text{overburden}}, x_i \in B_3 \\ \sigma_{ij} n_j = 0, x_i \in B_5 \end{cases} \quad (15)$$

where x_i is the Cartesian coordinates; $\sigma_{\text{overburden}}$ the weight of the overburden strata implicitly accounted in the model; n_j the components of a normal vector; and δ_{ij} the Kronecker delta.

The hydraulic support line is modelled by a pressure zone (2 MPa) moving towards the longwall face retreat occupying 5 cells behind the face (3.5 m). The hydraulic support pressure value is generally chosen close to the lithostatic pressure in order to support the rocks near the face and not to produce an overload of the surrounding rocks.

At the time marked as the “End time of the gravitational state of stress formation” in Fig. 5c, the distribution of stress tensor components is the result of gravity forces. The total number of the elements (cells) is 900 and 510 in x and y direction, respectively; the mesh step is 70 cm, so the lateral and vertical dimensions of the computational domain are 630 and 357 m, respectively.

4. Results and discussion

4.1. Violation of virgin state of stress of rock mass

The numerical simulation of Seam 3 as an example shows that the virgin state of the rock mass is considerably disturbed when the longwall face retreat starts. The pressure patterns combined with patterns of accumulated damages for two consecutive time points of face retreat are shown in Fig. 5a and b. The red rectangles in Fig. 5a and b indicate the volume of extracted coal. The pressure range to negative values was specially re-scaled only in order to identify the regions of negative pressure, as potential regions of cracking (black and grey

regions in Fig. 5a and b). These patterns are typical for all seams at the onset of face advancement. The patterns show that the arch-shaped local regions of the rock mass, under and above the gob, experience negative pressure from the very beginning of extraction. The larger the extracted volume, the larger the regions of negative pressure.

The dependence of pressure on time in one of the immediate roof points was also recorded (Fig. 5c). After the onset of face retreat, the virgin state of stress due to gravity forces, which was formed in the point close to the mining chamber, is violated and changes the sign several meters after the face advancement. When the pressure becomes negative, indicating tensile loading of rocks, the fracture criterion might be met as it occurs in the monitored point (Fig. 5c). After the failure, the rocks experience a residual strength and cave. Then, obviously, $P = 0$. Before the caving of rocks, it is observed that some periodic pressure jumps caused by the advancing face (Fig. 5d).

If we look at the next stages of face advancement, it is seen that the propagation of localized bands of plastic deformation violates the stress state to a more significant extent. The growing gob volume gradually increases the hanging roof length and shifts the zone of negative pressure towards the surface. Thus, the fracture process gradually entrains the roof and forms an arch-shaped fracture-rich zone (Fig. 6). One can see that the bands of localized inelastic deformation, which contour the fracture-rich zone, follow the lines of the maximum tangential stress. Due to the arch effect, there is a transient contour, where the stress state changes its type and sign (Fig. 7). The Lode parameter characterizing the type of stress state was calculated. Its pattern illustrates that the band of localized plastic deformation butts against the zone of compressive stresses ($\mu_\sigma = 2(S_2 - S_3)/(S_1 - S_3) - 1$, $\mu_\sigma \rightarrow -1$, where S_1, S_2 and S_3 are the principal deviatoric stresses). The transient contour marked in Fig. 7 becomes an obstacle for band propagation towards the surface and leads to deviation from the initial path along the direction of the maximum pair tangential stress, which appears to be a more preferable path.

4.2. Features of damage accumulation for Seam 7

When all conditions listed in Section 3.1 for damage measure are satisfied, cohesion begins degrading in some point of the rock mass. Stress relaxation gives rise to energy redistribution. The amplification of stresses and hence the formation of a local critical state occurs in some neighbouring regions causing further rock failures (Fig. 8a–c). Together with the build-up of gob, this process helps in sustaining the damage accumulation. As a result, a large number of the bands of localized accumulated damage divide the main roof and overburden the strata into a hierarchically organized system of blocks of different scales (Fig. 8d).

The patterns for successive time points (Fig. 8a–d) indicate that the emerging localization bands are oriented both in the direction of maximum tangential stresses and in the sub-vertical and sub-horizontal manner. The latter bands are the regions of bed separation, while the former bands divide the layers into several blocks of different scales. A concurrent action of these two mechanisms results in failures. The localization bands oriented along the maximum tangential stresses tend to move towards the face zone of abutment pressure amplification. They form an “onion-ring” structure of localized damage. It is evident that

when the rock mass is in the virgin state of stress, one of the principal stress axes, oriented perpendicular to the direction of vertical stress, is directed horizontally in the absence of tectonic stresses. The simulation data shows that trajectories of the maximum principal stress undergo a horizontal-to-sub-vertical rotation when the extraction of coal starts. Fig. 8a–d also illustrate the process of maximum principal stress axis rotation. An increased gob, in turn, causes the increase of rocks volume where the maximum principal stress axis rotation takes place. This appears to be the key mechanism responsible for roof cavings.

4.3. Diagrams of abutment pressure

Abutment pressure is one of the geotechnical parameters having significant value in mining management. An extensive application of this parameter is accounted for by a large number of relatively simple ways to measure it, using the electric resistance, strain gauges, etc. The abutment pressure caused by the advancing face can be estimated by numerical simulation.

After analyzing the numerical simulation data, the maximum level of abutment pressure is observed about 1.5–2.5 m deep into the panel in front of the face prior to the first caving of the main roof. After the first caving, the drop of abutment pressure occurs, and there appears to be a plateau of maximum abutment pressure with small oscillations in the area of about 6–8 m deep into the panel in front of the face.

The abutment pressure diagrams for successive times of face retreat t_i (Fig. 9) show that the relative amplification (vertical stress concentration factor) lies in the range of 1.5–2.5. Following the first main roof caving, a decrease in the abutment pressure concentration is observed in front of the face (t_5 in Fig. 9), which implies a completed effective energy dissipation. Further, the concentration factor was relatively unchanged with small oscillations, i.e. it has a periodic character due to periodic roof cavings. It is notable that the abutment pressure influence extends to a distance as long as ≥150 m after the first caving of the main roof. The calculations also show that 1.5–2.5 m from the face deep into the panel coal deforms plastically (Fig. 10).

Qualitatively close results for abutment pressure diagrams and coal yielding in front of the face were obtained by [3,7,8].

4.4. Validation of steps of the first and periodic cavings against field observations

Figs. 11–14 illustrate the estimations of the first and periodic cavings of the roofs of four different seams. We combined the structural roof and floor models of the corresponding seams with the patterns of accumulated damage due to longwall mining. This has been done in order to get a deeper insight into the features of roof deformation and to better estimate the steps of cavings. Table 3 summarizes the data of numerical modelling and provides a comparison with the field data.

Fig. 15 illustrates the dependence of steps of the first roof caving on the main roof thickness. In the considered range of thicknesses, it is linear with a positive slope. This dependence demonstrates a strong influence of the features of bedding and especially the main roof thickness on the steps of caving. The simulations show that the estimated main roof thicknesses are in the range of the field data.

In our opinion, the case of Polosuhinskaya mine is the most interesting one, where the step of first roof caving is rather high in comparison with the other seams. The roof of Seam 29a is composed of a relatively thick sandstone layer. This is the case of a poorly self-cavable roof. The simulations show that the first detachment crack in the main roof occurs at a distance of about 30 m from the immediate roof. The thickness of the immediate roof layer is also very large in comparison with other seams. Seam 29a belongs to the Lower Balahonskaya formation when the periods of sedimentation were long. Obviously, a failure of such a large thickness of the main roof demands bigger spans of the hanging roof, which was proved by our simulations.

Generally, the simulation results give slightly overestimated values of the first step of caving, which are approximately 10%. We believe that such an agreement of the model results with the field data is quite good. A small misfit between the numerical estimations and reality is due to a general complexity of the problem, caused by a large number of input parameters: physical-mechanical properties, stratigraphy, etc.

At the same time, the agreement between the numerical estimations of steps of periodic caving is much worse (Fig. 16). Values of the periodic steps are significantly underestimated due to: (1) After the first main roof caving, the face retreat rate generally increases by up to 30–40% of its initial rate. An increase in the retreat rate is likely to cause caving step growth. The change of the face retreat rate is not included into account; (2) After the first caving of the rocks, the gob properties recover with increasing distance behind the face. The recovery of the gob properties has not been included for consideration.

5. Conclusions

The main goal of this work has been to estimate steps of the first and periodic cavings of the main roof for several coal seams of the Kondomsky deposit (Kuznetsk Basin) versus the main roof thickness. It has been found that the caving distances estimated by the model are linearly related to the field observations. The estimated misfit between the numerical and field data is within 11%.

The numerical simulations show that the main goal has been achieved due to: (1) By inclusion of the borehole log, the features of bedding are among the key factors responsible for failure characteristics; (2) All physical-mechanical properties of rocks used in the simulation have been obtained in the experiments; (3) The mathematical model under development has been validated, relying on the field data on the steps of the first main roof caving.

Other results, e.g. yielding of coal in front of the face and abutment pressure diagrams, are in qualitative and quantitative agreement with the data of other researchers and other mines. The current limitations of the model are due to a disregarded increase in the face retreat rate and recovery of the gob properties after the first caving. These will be addressed in our future work, which would help to improve the estimations of periodic steps of caving. We are also planning to use the model under development for 3D numerical simulations of the

state of stress and strain evolution during longwall mining and for analyzing the gate and protective pillar stability.

Acknowledgements

This work was supported by the Russian Science Foundation, under grant 19-71-00083. Authors also would like to express gratitude to an anonymous reviewer whose comments helped to improve the quality of paper, and editors of the journal.

References

[1]. Zhang N, Zhang N, Han C, Qian D, Xue F. Borehole stress monitoring analysis on advanced abutment pressure induced by longwall mining. Arabian J Geosci 2014;7(2):457–63.

[2]. Wang J, Jiang J, Li G, Hu H. Exploration and numerical analysis of failure characteristic of coal pillar under great mining height longwall influence. Geotech Geol Eng 2016;34(2):689–702.

[3]. Islavath SR, Deb D, Kumar H. Numerical analysis of a longwall mining cycle and development of a composite longwall index. Int J Rock Mech Min Sci 2016;89:43–54.

[4]. Shabanimashcool M, Li CC. A numerical study of stress changes in barrier pillars and a border area in a longwall coal mine. Int J Coal Geol 2013;106:39–47.

[5]. Xie JL, Xu JL. Effect of key stratum on the mining abutment pressure of a coal seam. Geosci J 2017;21(2):267–76.

[6]. Wang S, Lia X, Wang S. Separation and fracturing in overlying strata disturbed by longwall mining in a mineral deposit seam. Eng Geol 2017;226:257–66.

[7]. Meng Z, Shi X, Li G. Deformation, failure and permeability of coal-bearing strata during longwall mining. Eng Geol 2016;208:69–80.

[8]. Guo H, Yuan L, Shen B, Qu Q, Xue J. Mining-induced strata stress changes, fractures and gas flow dynamics in multi-seam longwall mining. Int J Rock Mech Min Sci 2012;54:129–39.

[9]. Palchik V Formation of fractured zones in overburden due to longwall mining. Environ Geol 2003;44(1):28–38.

[10]. Sui W, Hang Y, Ma L, Wu Z, Zhou Y, Long G, et al. Interactions of overburden failure zones due to multiple-seam mining using longwall caving. Bull Eng Geol Environ 2015;74(3):1019–35.

[11]. Kang H, Lou J, Gao F, Yang J, Li J. A physical and numerical investigation of sudden massive roof collapse during longwall coal retreat mining. Int J Coal Geol 2018;188:25–36.

[12]. Tulu IB, Esterhuizen GS, Gearhart D, Klemetti TM, Mohamed KM, Sub DWH. Analysis of global and local stress changes in a longwall gateroad. Int J Min Sci Technol 2018;28(1):127–35. [PubMed: 30733889]

[13]. Ju Y, Wang Y, Su C, Zhang D, Ren Z. Numerical analysis of the dynamic evolution of mining-induced stresses and fractures in multilayered rock strata using continuum-based discrete element methods. Int J Rock Mech Min Sci 2019;113:191–210.

[14]. Esterhuizen GS, Gearhart DF, Klemetti T, Dougherty H, van Dyke M. Analysis of gateroad stability at two longwall mines based on field monitoring results and numerical model analysis. Int J Min Sci Technol 2019;29(1):35–43.

[15]. Wang H, Jiang Y, Zhao Y, Zhu J, Liu S. Numerical investigation of the dynamic mechanical state of a coal pillar during longwall mining panel extraction. Rock Mech Rock Eng 2013;46(5):1211–21.

[16]. Shabanimashcool M, Li CC. Numerical modelling of longwall mining and stability analysis of the gates in a coal mine. Int J Rock Mech Min Sci 2012;51:24–34.

[17]. Khanal M, Guo H, Adhikary D. 3D numerical study of underground coal mining induced strata deformation and subsequent permeability change. Geotech Geol Eng 2019;37(1):235–49.

[18]. Liu C, Li HM, Jiang DJ. Numerical simulation study on the relationship between mining heights and shield resistance in longwall panel. Int J Min Sci Technol 2017;27(2):293–7.

[19]. Makarov PV, Smolin IY, Evtushenko EP, Trubitsyn AA, Trubitsyna NV, Voroshilov SP. Evolution scenarios of the rock mass over the opening. Fiz Mezomekh 2009;12(1):65–82.

[20]. Jones NS. A review of the AMM & CMM resources in the Kuznetsk (Kuzbass) Coal Basin, Russia. Brit Geol Survey 2005:48.

[21]. Yavorskii VI. Geology of coal deposits and oil shale of the USSR Volume 7 In: Proceedings of Kuznetsk, Gorlovsky basins and other coal deposits of Western Siberia. Nedra; 1969 p. 912.

[22]. Wilkins ML. Computer simulation of dynamic phenomena. Springer Science & Business Media; 1999 p. 266.

[23]. Taiwo AO. Design and stability of barrier pillars in longwall mining. Master's dissertation. Virginia: Virginia Polytechnic Institute and State University; 1982 p. 165.

[24]. Drucker DC, Prager W. Soil mechanics and plastic analysis or limit design. Q Appl Math 1952;10(2):157–65.

[25]. Stefanov YP, Evseev VD, Bakeev RA. Numerical modelling of deformation and fracture in geomaterials. Fiz Mezomekh 2004;7(S2):265–8.

[26]. Kapustyanskii SM, Nikolaevskii VN, Zhilenkov AG. Nonholonomic model of deformation of highly porous sandstone under its internal crushing. Izv Phys Solid Earth 2010;46(12):1095–104.

[27]. Stefanov YP, Bakeev RA. Formation of flower structures in a geological layer at a strike-slip displacement in the basement. Izv Phys Solid Earth 2015;51(4):535–47.

[28]. Psakhie SG, Shilko EV, Grigoriev AS, Astafurov SV, Dimaki AV, Smolin AY. A mathematical model of particle-particle interaction for discrete element based modeling of deformation and fracture of heterogeneous elastic-plastic materials. Eng Fract Mech 2014;130:96–115.

[29]. Makarov PV, Eremin MO, Kostandov YA. Prefracture time of gabbro specimens in a damage accumulation model. Phys Mesomech 2014;17(3):199–203.

[30]. Alejano LR, Alonso E. Considerations of the dilatancy angle in rocks and rock masses. Int J Rock Mech Min Sci 2005;42(4):481–507.

[31]. Hoek E, Brown ET. Practical estimates of rock mass strength. Int J Rock Mech Min Sci 1997;34(8):1165–86.

[32]. Kachanov LM. Time of the rupture process under creep conditions, Izy Akad. Nank SSR Otd Tech Nauk 1958;8:26–31.

[33]. Rabotnov YN. Kinetics of creep and creep rupture In: Proceedings of irreversible aspects of continuum mechanics and transfer of physical characteristics in moving fluids. Vienna: Springer; 1968 p. 326–34.

[34]. Mazars J, Pijaudier-Cabot G. From damage to fracture mechanics and conversely: a combined approach. Int J Solids Struct 1996;33(20–22):3327–42.

[35]. Sahara DP, Schoenball M, Gerolymatou E, Kohl T. Analysis of borehole breakout development using continuum damage mechanics. Int J Rock Mech Min Sci 2017;97:134–43.

[36]. Kostandov YA, Makarov PV, Eremin MO, Smolin IY, Shipovskii IE. Fracture of compressed brittle bodies with a crack. Int Appl Mech 2013;49(1):95–101.

[37]. Smolin IY, Makarov PV, Kulkov AS, Eremin MO, Bakeev RA. Blow-up modes in fracture of rock samples and earth's crust elements. Phys Mesomech 2018;21(4):297–304.

[38]. Makarov PV, Evtushenko EP, Eremin MO. Evolution of the state of stress and strain of the rock mass with excavations Mathematical Modeling. Tomsk: Publishing House of Tomsk State University; 2016 p. 184.

[39]. Alejano LR, Bobet A. Drucker-prager criterion. Rock Mech Rock Eng 2012;45(6):995–9.

[40]. Olkhovatenko VE. Engineering geology of coal deposits of the Kuznetsk basin. Tomsk: Publishing house of Tomsk State University of Architecture and Building; 2014 p. 150.

[41]. Hoek E, Martin CD. Fracture initiation and propagation in intact rock – a review. J Rock Mech Geotech Eng 2014;6(4):287–300.

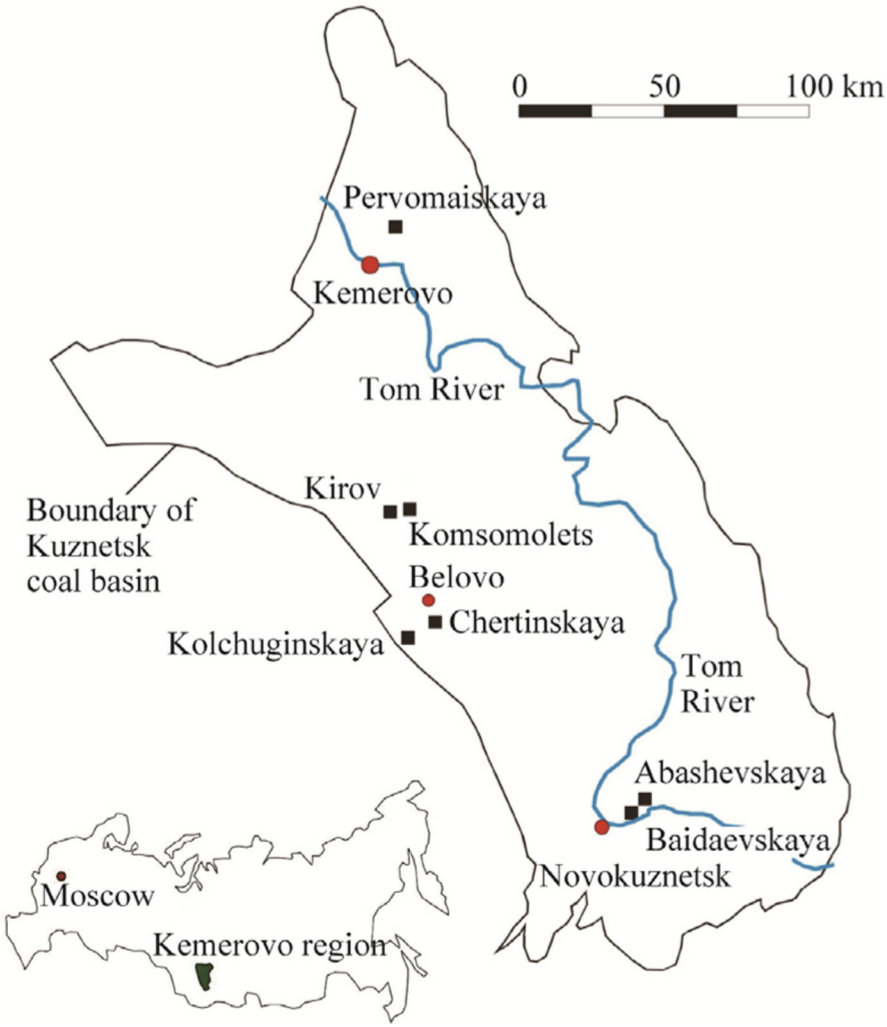

Fig. 1.
Location and the outer boundary of the Kuznetsk Basin (after [20]).

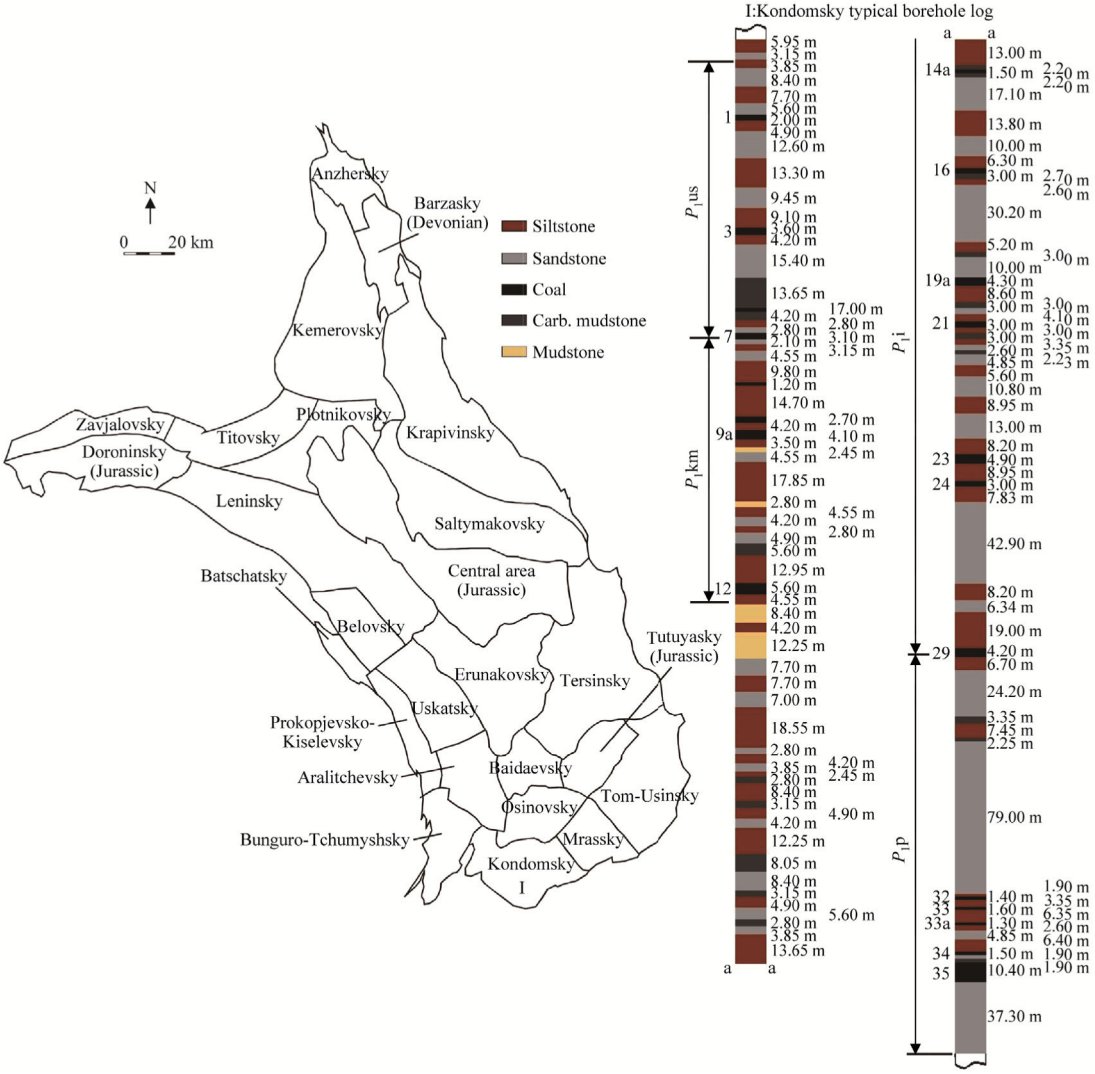

Fig. 2.

Division of the Kuznetsk Basin into exploration deposits (after [20,21]).

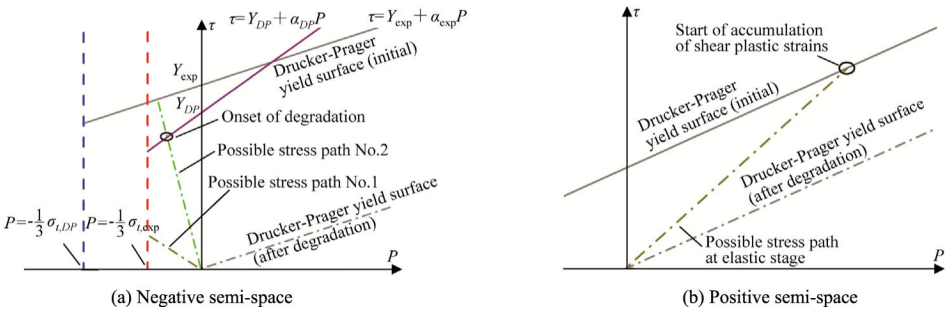

Fig. 3.

Illustration of the calculation procedure of damage accumulation measure.

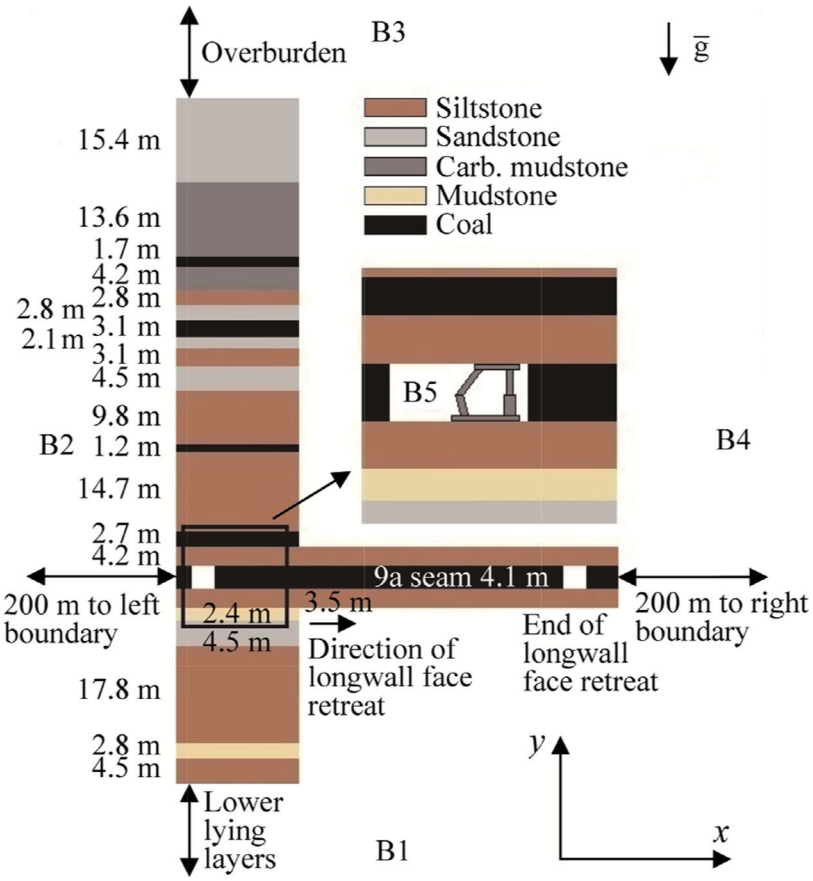

Fig. 4.

Roof and floor model and loading and mining schemes for Seam 9a of the Kondomsky deposit.

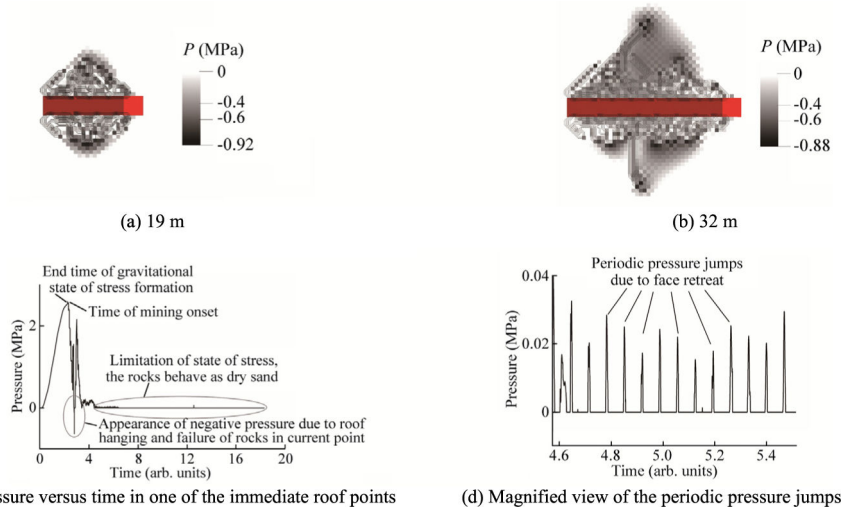

Fig. 5.

Combined pattern of pressure and accumulated damage for consecutive times of face retreat for Seam 3.

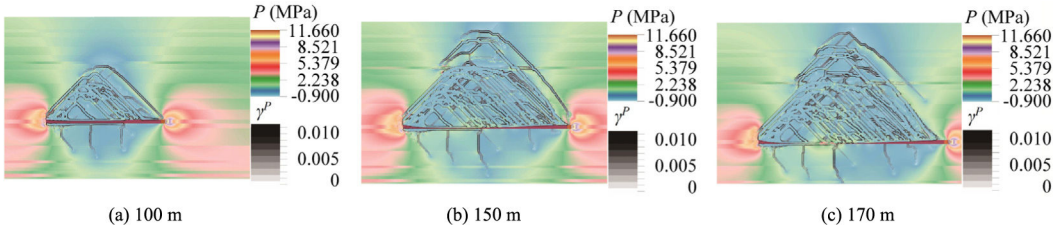

Fig. 6.

Combined patterns of pressure and wireframe representation of equivalent plasticstrain (γ^P) for successive times of face retreat. The dark red region indicates the gob.

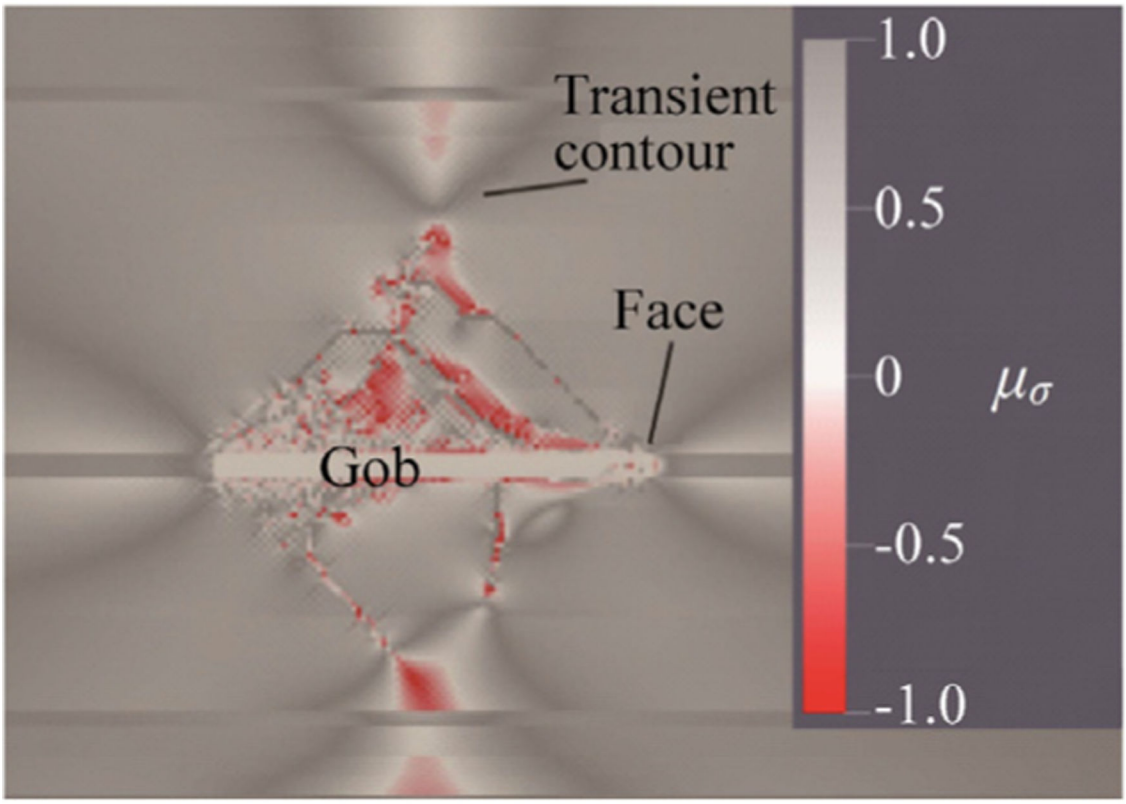

Fig. 7.
Pattern of Lode parameter illustrating the obstacle transient contour (dark grey isoline) of compressive stresses with face retreat being 50 m.

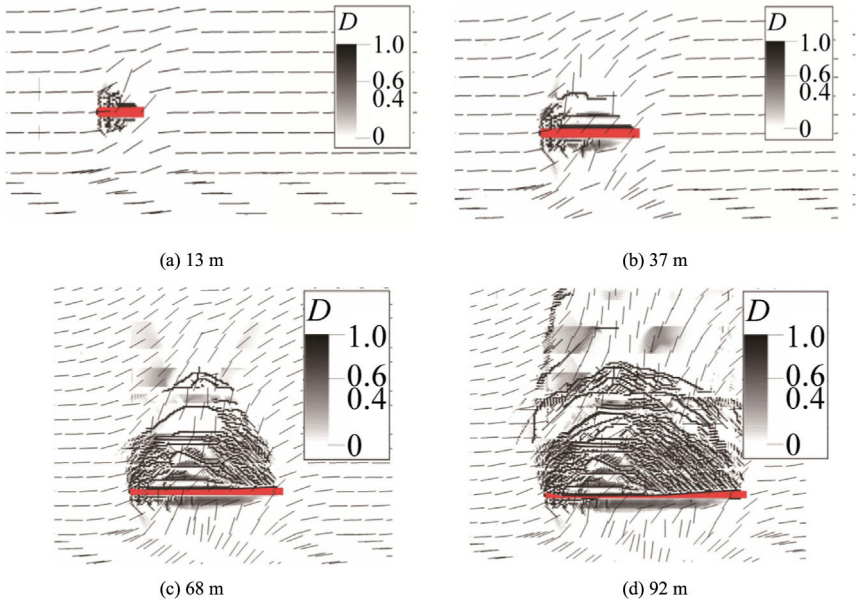

Fig. 8.

Accumulated damage in rock mass elements and stages of the maximum principal stress axis rotation (arrows without heads) for different face retreats.

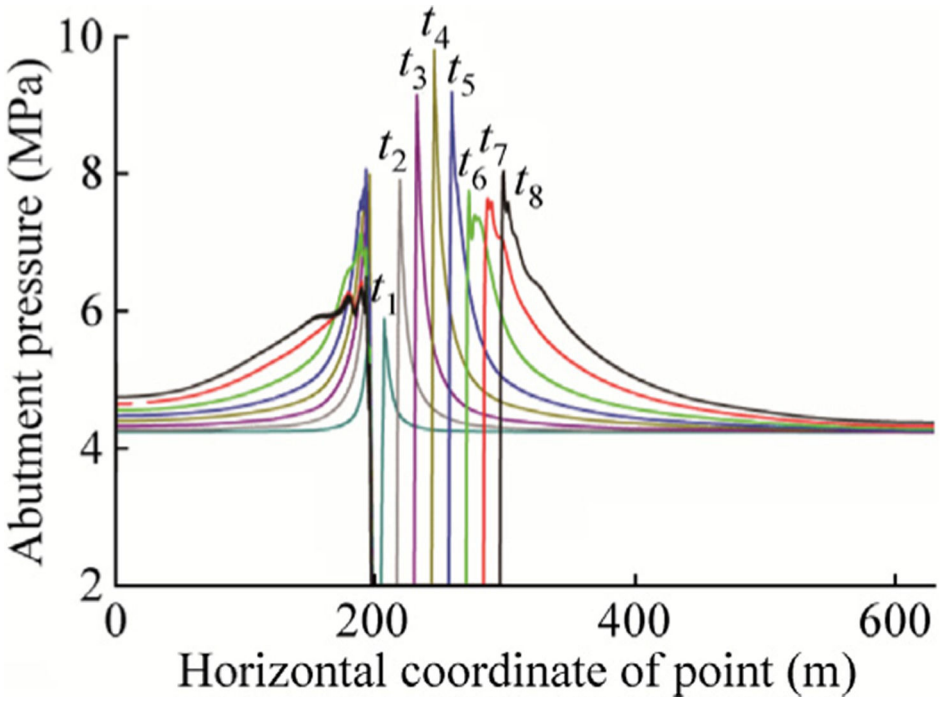

Fig. 9.

Abutment pressure diagrams for different times of face retreat: t_1 (5 m), t_2 (16 m), t_3 (30 m), t_4 (43 m), t_5 (56 m), t_6 (69 m), t_7 (82 m), and t_8 (95 m) at the horizon of the coal seam.

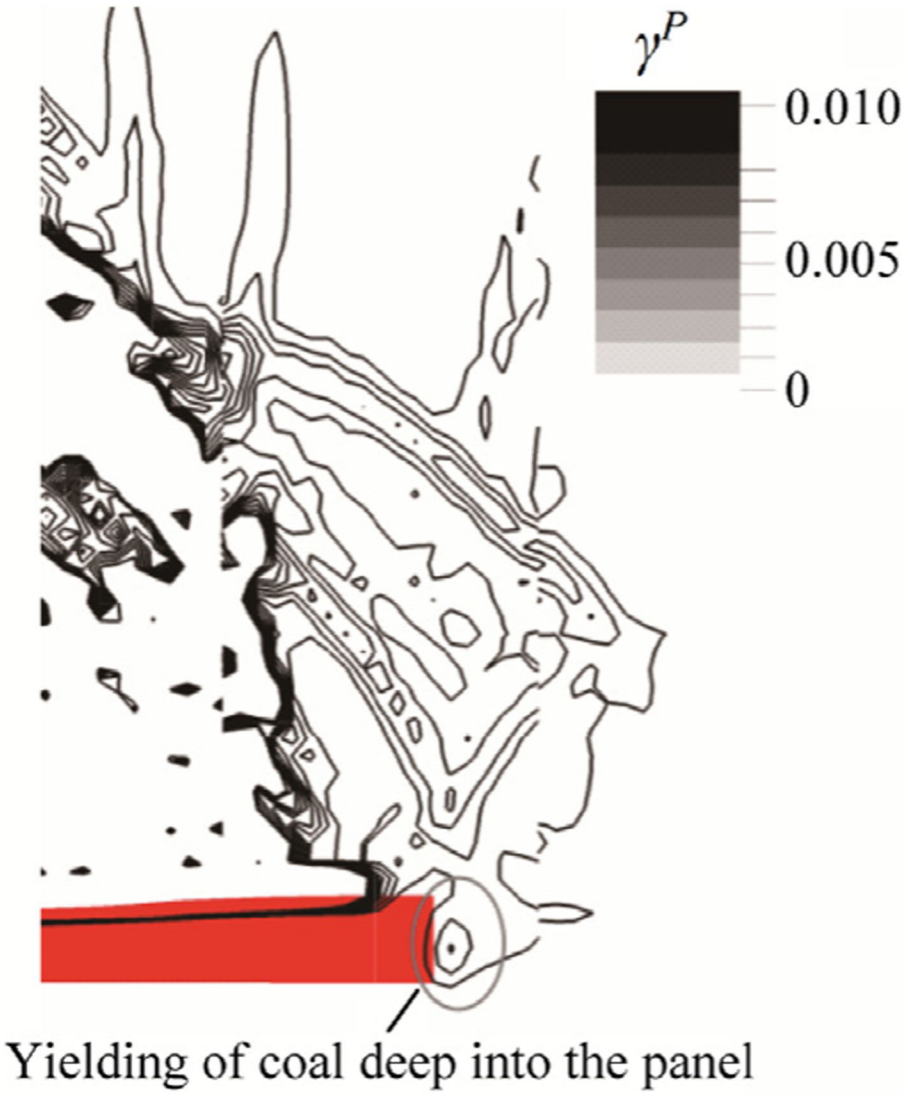

Fig. 10.
Pattern of equivalent inelastic strain (wireframe) demonstrating coal yielding in front of the face deep into the pillar.

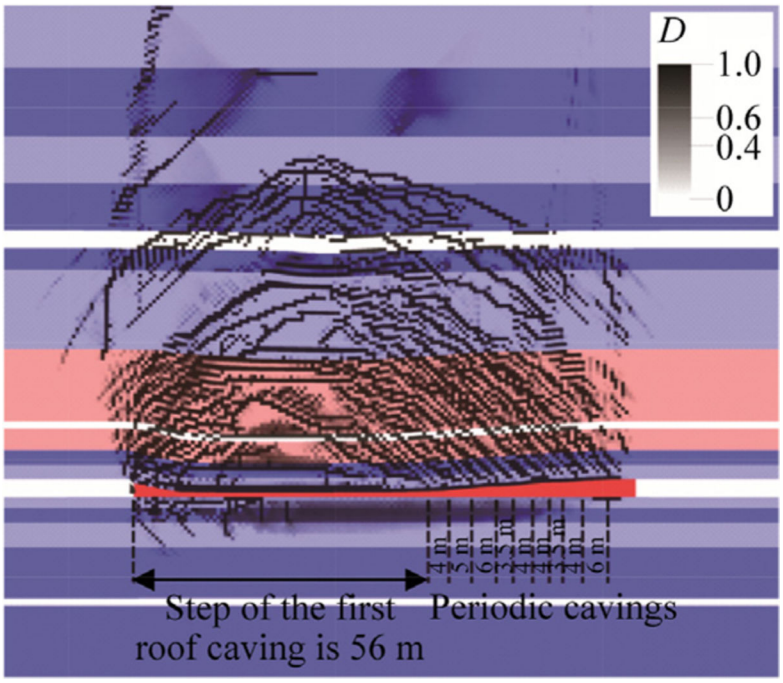

Fig. 11.
Estimation of steps of the first and periodic main roof cavings of Seam 7.

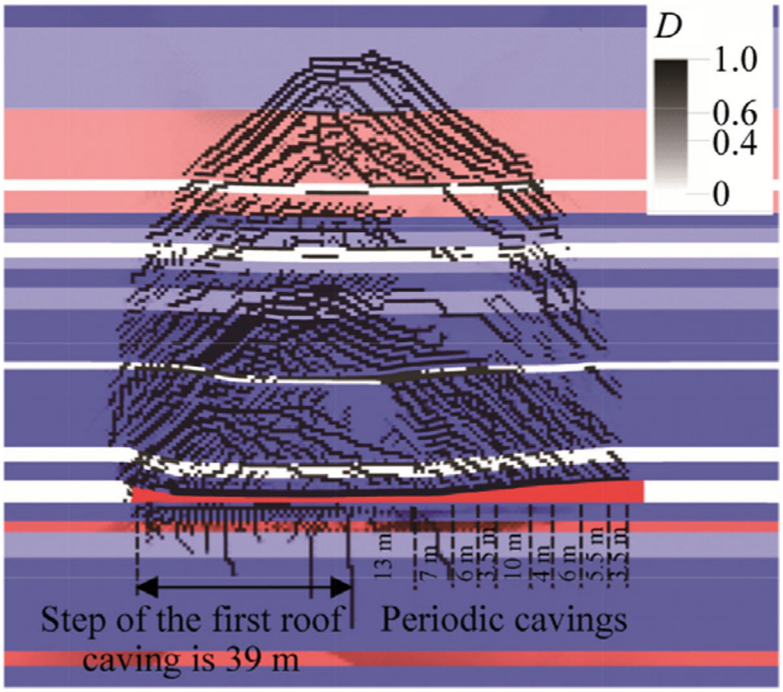

Fig. 12.
Estimation of steps of the first and periodic main roof cavings of Seam 9a.

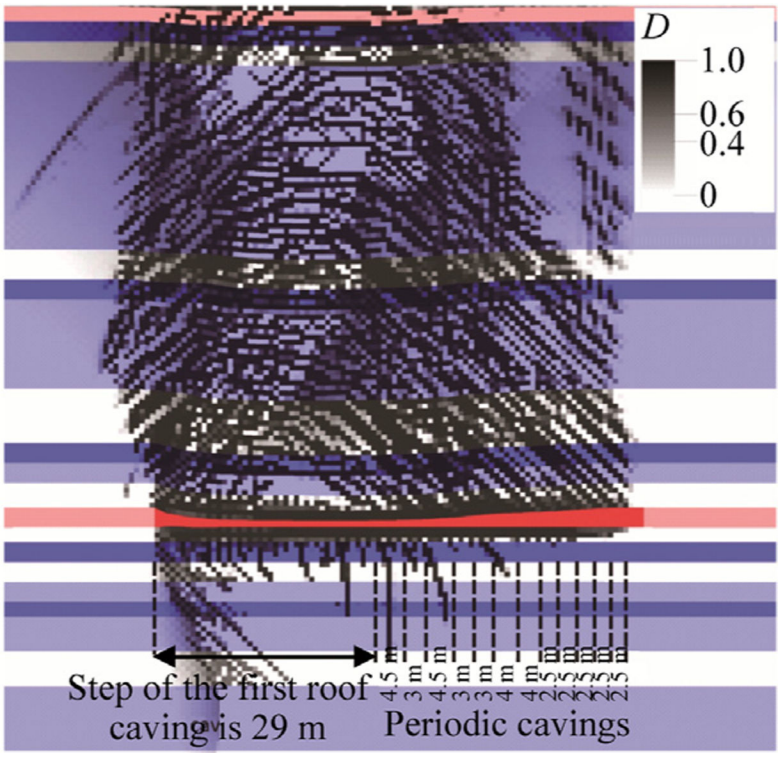

Fig. 13.
Estimation of steps of the first and periodic main roof cavings of Seam 21.

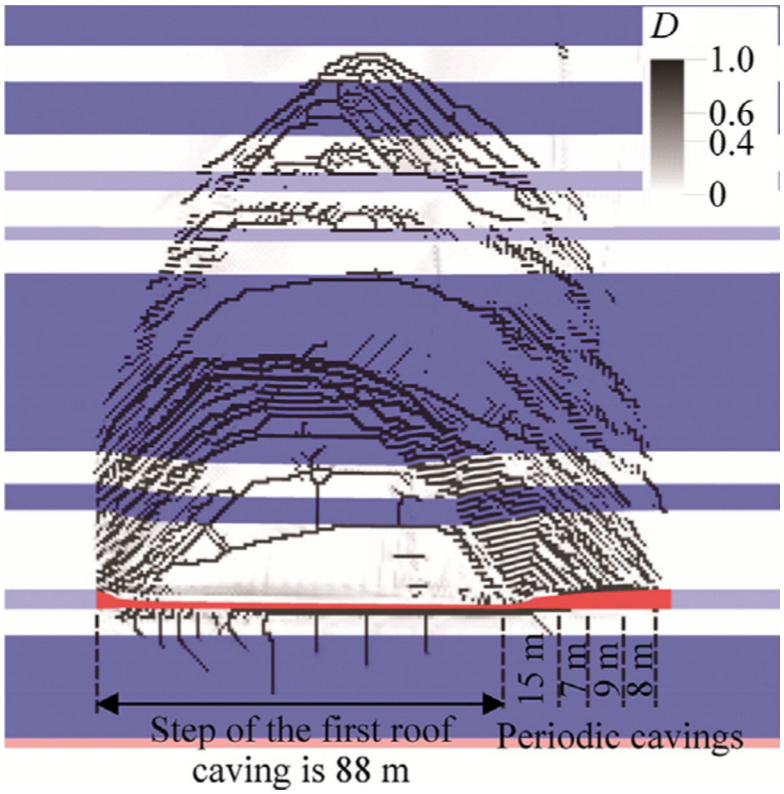

Fig. 14.
Estimation of steps of the first and periodic main roof cavings of Seam 29a.

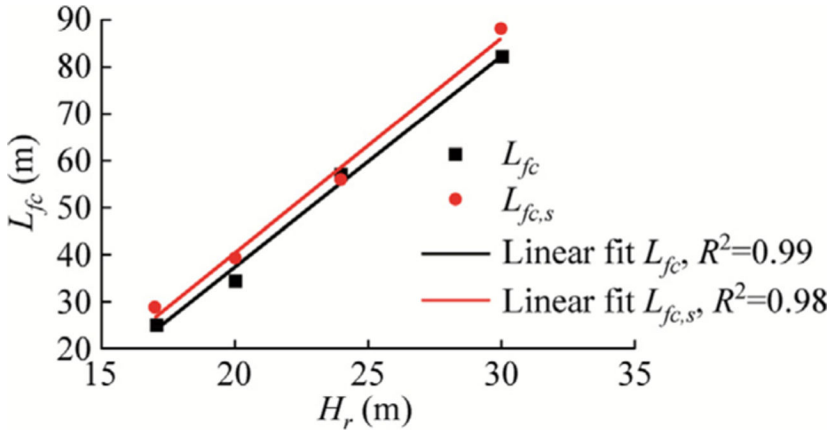

Fig. 15.
Summary graph of estimation of steps of the first main roof caving.

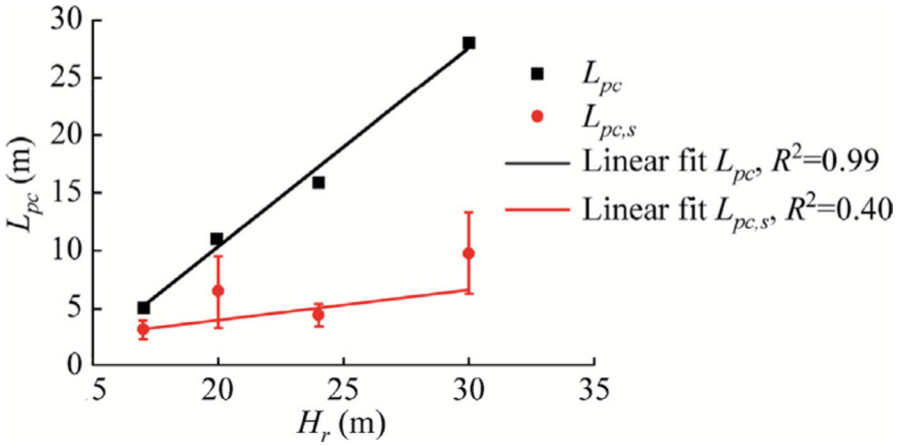

Fig. 16.
Summary graph of estimation of steps of periodic main roof cavings.

Table 1

Strength characteristics of rocks of the Kondomsky deposit [40].

Rock	$\sigma_{t,\exp}$ (MPa)	$\sigma_{t,DP}$ (MPa)	$\sigma_{c,\exp}$ (MPa)	$Y_{\exp}$ (MPa)	Y_{DP} (MPa)	$\alpha_{\exp}$	α_{DP}
Sandstone	0.94	1.545	2.84	1.15	0.815	0.5	0.87
Siltstone	0.63	1.369	1.863	1.01	0.543	0.48	0.86
Mudstone	0.3	1.064	0.93	0.82	0.262	0.58	0.89
Carb. mudstone	0.5	1.06	1.51	0.7	0.43	0.55	0.87
Coal	0.37	0.408	1.19	0.3	0.326	0.47	0.91

Notes: $\sigma_{t,\exp}$ is the experimental uniaxial tensile strength; $\sigma_{t,DP}$ the calculated uniaxial tensile strength; $\sigma_{C,\exp}$ the experimental uniaxial compressive strength; $Y_{\exp}$ the experimental cohesion; Y_{DP} the calculated cohesion; $\alpha_{\exp}$ the experimental internal friction factor; and α_{DP} the calculated internal friction factor.

Table 2

Density, elastic properties and dilatancy factor of rocks [40].

Rock	ρ_0 (g/cm^3)	K (GPa)	μ (GPa)	Λ
Sandstone	2.54	8.729	7.45	0.0625
Siltstone	2.55	9.412	6.55	0.06
Mudstone	2.46	9.255	5.95	0.0725
Carb. mudstone	1.93	8.4	5.4	0.069
Coal	1.29	2.35	1.625	0.059

Notes: ρ_0 is the reference value of density; K the bulk modulus; μ the shear modulus; and Λ the dilatancy factor.

Table 3

Field data on steps of the main roof caving for several mines of South Kuzbass in comparison with numerical simulation data.

Mine	v_f (m/day)	t^* (a.u.)	L_{fc} (m)	$L_{fc,s}$ (m)	L_{pc} (m)	$L_{pc,s}$ (m)	H_r (m)	Seam	H_d (m)	$H_{d,s}$ (m)
Raspadskaya 1	4.3	13.25	57	56	16	3.5–6	24	7	280–425	300
Raspadskaya 2	9.3	3.76	35	39	10–12	3.5–13	20–38	9a	197–318	200
Alardinskaya	5	5	25	29	28	7–15	17–20	21	160–260	200
Polosuhinskaya	6	13.66	82	88	28	2.5–4.5	20–50	29a	250–350	300

Notes: v_f is the face retreat rate; t^* the adjusted time of a fracture incubation process in the model; L_{fC} the step of the first main roof caving; $L_{fC,S}$ the step of the first main roof caving in simulation; L_{pC} the step of the periodic main roof caving; $L_{pC,S}$ the step of the periodic main roof caving in simulation; H_r the thickness of main roof; H_d the depth of the coal seam; and $H_{d,S}$ the depth of the coal seam in simulation.